ACS OMEGA

http://pubs.acs.org/journal/acsodf

Article

Optical and Electrical Transport Evaluations of n-Type Iron Pyrite Single Crystals

Shunsuke Uchiyama, Ryosuke Sato, Ryoji Katsube, Muhammad Monirul Islam, Hideaki Adachi, Takeaki Sakurai, Yoshitaro Nose, and Yasuaki Ishikawa*

Cite This: *ACS Omega* 2021, 6, 31358−31365

Read Online

ACCESS | Metrics & More | Article Recommendations

ABSTRACT: Iron pyrite [cubic FeS_2 ($cFeS_2$)] is considered as an earth-abundant and low-cost thin-film photovoltaic material. However, the conversion efficiency of $cFeS_2$-based solar cells remains below 3%. To elucidate this limitation, we evaluate the optical and electrical characteristics of $cFeS_2$ single crystals that are grown using the flux method, thus providing us an understanding of the electron transport behavior of $cFeS_2$ single crystals. The oxide layer on the surface of $cFeS_2$, which can possibly have an influence on the electrical characteristics of $cFeS_2$, is removed prior to characterization *via* optical spectroscopy and electrical transport measurement. The optical property of $cFeS_2$ was found to have both indirect and direct transitions. We also observed the presence of a band tail below the conduction band. The obtained electrical transport behavior indicates that $cFeS_2$ bulk exhibits a high defect density and a disordered phase, thus leading to the hopping conduction mechanism. Our results will pave the way for the development of photovoltaic applications with iron pyrite.

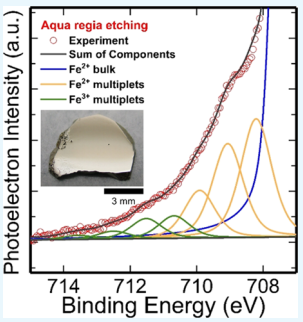

1. INTRODUCTION

Iron pyrite [cubic FeS_2 ($cFeS_2$)] has been recognized as a semiconductor that exhibits excellent potential as a photovoltaic (PV) material since it has a band gap of about 0.95 eV. Such a band gap value is suitable for PV application. In addition, $cFeS_2$ exhibits a particularly remarkable optical absorption characteristic [optical absorption coefficient (α) > 10^5 cm^{-1} above 1.2 eV].[1,2] This characteristic indicates that a film thickness of about 100 nm can absorb 90% or more of the incident sunlight. Bulk n-type $cFeS_2$ single crystals can have high majority carrier diffusion lengths (L = 0.1−1 μm).[2−5] $cFeS_2$ is also composed of iron (Fe) and sulfur (S), which are considered as rare metal-free and nontoxic elements.[6] Wadia *et al.* have calculated the cost of several materials for PV application, with the assumption that each material has reached the theoretical limit of its conversion efficiency. They also showed that $cFeS_2$ is the best candidate among the solar cell materials in terms of cost and efficiency. This indicates that owing to the characteristics of $cFeS_2$, such as its abundance on earth and high optical absorption, it can be used as a solar cell absorber. Since $cFeS_2$ materials possess these promising properties, they have been synthesized by using a wide range of methods, such as chemical vapor transport (CVT),[7] chemical vapor deposition,[8−12] and thermal sulfurization of various precursor materials,[13−18] nanowires,[19] and colloidal nanocrystals.[20−22]

Despite the extensive efforts for synthesis and investigation of the material, $cFeS_2$ thin films still exhibit poor properties for use in a PV device.[22−24] $cFeS_2$ single crystals used in PV devices have obtained a conversion efficiency of 2.8%.[3] Their report used a photoelectrochemical device structure using unintentionally doped n-type $cFeS_2$ single crystals fabricated using the CVT growth method and an iodine/iodide aqueous electrolyte.[3] An outstanding photocurrent of 42 mA/cm^2, which is used as a short-circuit current density (J_{SC}), was obtained; however, the efficiency was ultimately limited by a low open-circuit voltage ($V_{OC} \leq$ 187 mV) and moderate fill factor (FF ∼ 50%).[3] The lack of important synthetic details and specific discussion on the factors for controlling the performance of these solar devices has restricted the understanding of $cFeS_2$ materials. Therefore, understanding the reason for their low performance is important to improve the performance of PV devices using $cFeS_2$.

Recently, some issues, such as surface states and doping into the bulk, have emerged. X-ray photoelectron spectroscopy (XPS) was used to observe the surface inversion of $cFeS_2$ single crystals, which suggests the pinning of the Fermi level near the valence band edge at the surface.[25,26] This provides a reasonable explanation for the cause of the low V_{OC} of $cFeS_2$ used in PV devices. These surface conditions have been modeled by the ligand field theory (LFT) based on the Fe−S

Received: September 21, 2021
Accepted: October 28, 2021
Published: November 11, 2021

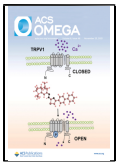

coordination.[27] The reduction of the Fe−S coordination at the surface region leads to the formation of the intrinsic defect states at the valence band edge, which leads to Fermi level pinning and subsequent band bending.[3,27,28] The LFT modeling presented the low photovoltages of metal/n-$cFeS_2$ junctions that create leaky tunnel barriers.[3,27,28] However, the experimental evidence provided by the LFT modeling has not yet been validated.

On the other hand, recent progress has been made to understand the electronic transport in $cFeS_2$ single crystals and FeS_2 thin films.[19,22,29−37] Especially, Limpinsel *et al.* observed surface-dominated conduction at low temperature in polished flux-grown $cFeS_2$ single crystals, suggesting that the bulk n-type carriers presented less effect in the conduction mechanism.[29] Based on the XPS discussion,[25−27] Limpinsel *et al.* concluded that this surface-dominated conduction which was likely p-type was derived from the surface Fermi level pinned near the valence band maximum in FeS_2 single crystals.[29] However, the Hall effect measurements shown by Limpinsel *et al.* as evidence of a p-type inversion layer showed that the Hall coefficient itself was not clearly inverted but fluctuated between small positive and negative values at lower temperatures. Thus, there remains uncertainty as to whether the surface layer is definitively p-type or not. Furthermore, the surface-dominated conduction at a low temperature has very low conductivity; therefore, this conduction has a possibility of Efros−Shklovskii variable range hopping.[32−35]

Additionally, Walter *et al.* also have reported the existence of surface conduction of $cFeS_2$ single crystals by Hall effect measurement in cryostats equipped with 9 T superconducting magnets, from 1.5 to 300 K.[30] They indicated that the transport, which is clearly different from that of the bulk, usually occurs in a region limited to within 2−3 nm from the surface. They demonstrated that the surface conduction of $cFeS_2$ single crystals was truly two-dimensional, and the surface region established a p-type surface inversion layer, which suggested no possible artifacts from hopping conduction. Through nonlinear Hall effect at temperature-dependent behavior, bulk-to-surface crossover was expected.[30]

Furthermore, recent efforts have identified that sulfur vacancies (V_S), which exist on the surface and the bulk, also influence electron transport. Limpinsel *et al.* and Voigt *et al.* suggested that these V_S at the bulk of FeS_2 limited the PV performance.[29,31] Particularly, Voigt *et al.* revealed that V_S act as deep donors in the bulk from the extensive electrical transport measurements of high-quality $cFeS_2$ crystals.[31] They also reported that crystals have grown *via* CVT under decreasing sulfur vapor pressure, which can help increase V_S, reduce the bulk resistivity, increase the electron density, and reduce the activation energy of transport and onset of the positive temperature coefficient of resistance. They also indicated that V_S are native defects affecting the electrical transport of $cFeS_2$ bulk.

As previously discussed, numerous research studies on $cFeS_2$ for PV application have been conducted. However, their electron transport behaviors, including surface states, are still unclear. The conventional $cFeS_2$ single crystals have oxide layers at the surface, which formed after the wafer preparation. However, the influence of this oxide layer on the electrical transport has not yet been elucidated. Here, we investigated the optical and electrical characteristic properties of $cFeS_2$ single crystals after the removal of the oxide layer that formed after the wafer preparation. The aqua regia treatment was performed to remove the oxide layer on the $cFeS_2$ crystal. This process is an original treatment in this study as a surface treatment of the $cFeS_2$ crystal.

2. RESULTS AND DISCUSSION

2.1. Structural and Chemical Characterization. Figure 2a presents the X-ray diffraction (XRD) profile of the powder of the grown crystal of $cFeS_2$ shown in Figure 1. Each strong peak in the profile was assigned by the reference pattern of $cFeS_2$ (ICDD# 00-042-1340). Figure 2b presents the XRD profile of the crystal facet that appeared during the crystal growth, which is presented in Figure 1a. The two peaks were assigned to the (111) and (222) planes according to the reference pattern of $cFeS_2$ (ICDD# 00-042-1340), indicating that the grown crystal corresponds to the $cFeS_2$ single crystal. However, we could not detect any XRD profiles from the $cFeS_2$ wafers after slicing and polishing (Figure 1b), indicating that the crystal facet of the prepared sample is not accurately controlled in this study.

Table 1 presents the results of the quantitative analysis (molar ratios) measured using the electron probe micro-analyzer (EPMA) for the ratio of Fe and S in the grown $cFeS_2$ single-crystal wafers (five different wafers). For this analysis, three measurement points were selected per sample. As presented in Table 1, the molar ratios of Fe and S were on average 33.35−33.57 and 66.43−66.65%, respectively. The EPMA usually has a relative error of about a few percent, suggesting that the molar ratio for samples 1−5 shown in Table 1 has almost the same value. The molar ratio of Fe and S was found to be very close to the stoichiometric ratio (Fe/S = 1:2). In addition, no other elements except Fe and S were detected in the analysis.

Figure 3 presents the Raman spectra of the $cFeS_2$ single-crystal wafer treated after aqua regia etching. As demonstrated in Figure 3, three sharp peaks were confirmed at 343, 377, and 430 cm^{-1}. Usually, $cFeS_2$ has three peaks corresponding to the active modes of $cFeS_2$ of the S_2 vibration (E_{ge}) mode at 343 cm^{-1}, S−S in-phase stretch (A_{ge}) mode at 377 cm^{-1}, and coupled vibration and stretch ($T_{ge(3)}$) mode at 430 cm^{-1} in the Raman spectra.[29,32,38] The intensity of the E_{ge} peak was a little bit higher than that of A_{ge}, which is not fluently observed in the references, but each peak position observed in our experiment matched well the reference date, and the other phases, such as FeS_2 marcasite and pyrrhotite, were not detected.

Figure 4a,b presents the comparison of the depth profiles of the O 1s spectrum *via* Ar^+ ion sputtering in the XPS system for the $cFeS_2$ single-crystal wafer after the surface chemical treatment. In our experiment, the etching rate is about 0.2

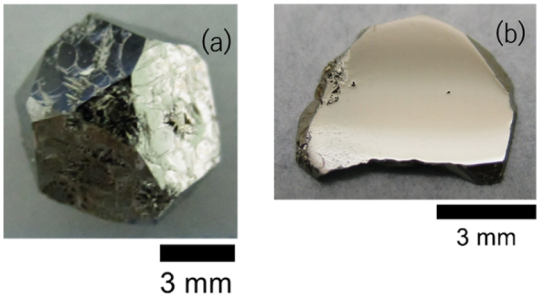

Figure 1. Typical photographs of the grown crystal (a) and typical photographs of the polished wafer of the grown crystal (b).

https://doi.org/10.1021/acsomega.1c05232
ACS Omega 2021, 6, 31358−31365

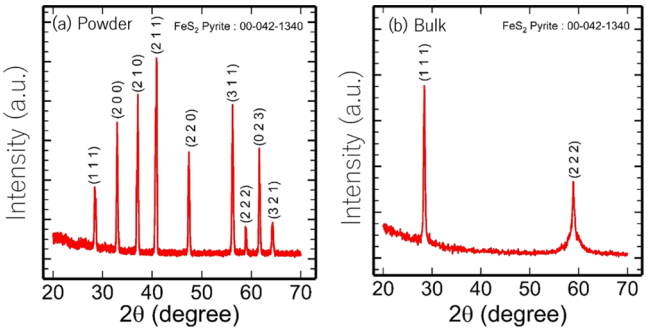

Figure 2. XRD profile of the powder made by crushing the grown crystal (a) and XRD profile of the appearing facet of the grown crystal (b).

Table 1. Molar Ratio (%) of Fe and S in the Grown $cFeS_2$ Single-Crystal Wafers

point	molar ratio (%)	sample 1	sample 2	sample 3	sample 4	sample 5
1	Fe	33.69	33.20	33.81	33.56	33.55
	S	66.31	66.80	66.19	66.44	66.45
2	Fe	32.82	33.70	33.26	33.33	33.53
	S	67.18	66.30	66.74	66.67	66.47
3	Fe	33.53	33.75	33.65	33.48	33.54
	S	66.47	66.25	66.35	66.53	66.46
ave.	Fe	33.35	33.55	33.57	33.46	33.54
	S	66.65	66.45	66.43	66.55	66.46

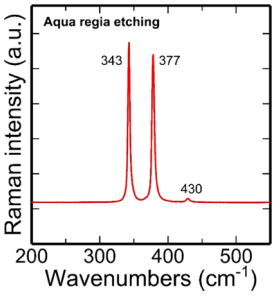

Figure 3. Typical Raman spectra of the $cFeS_2$ single crystal treated by aqua regia etching.

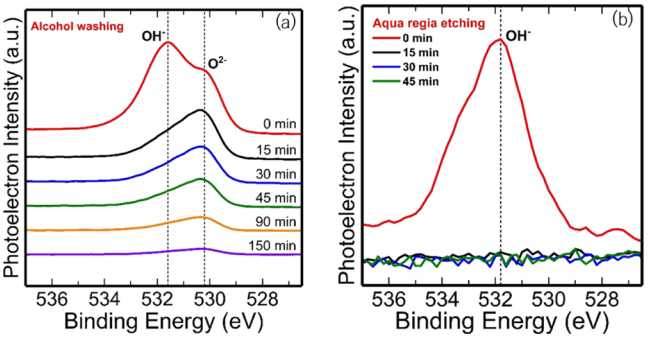

Figure 4. XPS depth profiles of O 1s for the iron pyrite $cFeS_2$ single-crystal wafer treated by alcohol washing (a) and aqua regia etching (b). The surface of the wafers was etched with Ar^+ ion gas for 150 min, and XPS measurement was performed every 15 min.

nm/s with a very low acceleration voltage of 500 eV. From Figure 4a, while the hydroxide (OH^-) species was immediately removed *via* Ar^+ ion sputtering, the oxide (O^{2-}) species was still confirmed after sputtering,[39] indicating that the alcohol washing cannot remove the oxide surface. Contrarily, Figure 4b presents the depth profiles of the O 1s spectrum of $cFeS_2$ single crystals treated with both alcohol washing and aqua regia etching. As presented in Figure 4b, the production of oxides, shown by O^{2-} species, was not detected. We also confirmed that the OH-related peak immediately disappeared completely after the Ar^+ ion sputtering. The results presented in Figure 4 confirmed that the relatively thick (>1 μm) oxide layer, which was formed after the wafer preparation, was removed after aqua regia etching. The air moisture will be absorbed at the surface of $cFeS_2$ due to its exposure to the atmosphere during the preparation for measurement. The Ar^+ ion sputtering was not performed in a shorter cycle for XPS analysis; it is hard to estimate the thickness of the native oxide. However, we presume that the thickness of the native oxide layer formed *via* environmental air exposure is not so thick since the electrical characterization was successfully performed as described in Section 2.2.

Figure 5a presents the S 2p spectrum of the sample treated with aqua regia etching. These spectra were fitted with S $2p_{3/2}$−S $2p_{1/2}$ spin−orbit doublets with a fixed intensity ratio of 2:1 and 1.2 eV separation, which are because of S_2^{2-} anions in iron pyrite.[40] Additionally, high binding energy shoulder features were observed at 164−167 eV, which corresponded to the satellite. Similar to other components, monosulfide (S^{2-}) at 161−164 eV was also observed in these spectra.[41] Figure 5b presents the Fe $2p_{3/2}$ spectrum of the sample treated with aqua regia etching. To analyze the high-resolution Fe 2p spectra, the Shirley background was used for the Fe $2p_{3/2}$ envelope. Moreover, the Fe $2p_{3/2}$ envelope obtained from the compounds containing a high-spin Fe cation was fitted by the peaks corresponding to the Gupta−Sen (GS) multiplets and satellites.[39,42,43] GS multiplets are patterns calculated by Gupta and Sen for the free ions of various transition metals.[44,45] They revealed that the number of unpaired electrons determines the number and intensity of the signal related to the multiplets, whereas the shift in the binding energy is a function of the atomic number.[44,45] Figure 5c presents the Fe $2p_{3/2}$ spectrum of $cFeS_2$ single crystals treated with aqua regia etching and the calculation result by linear fitting. From Figure 5c, it can be seen that the Fe $2p_{3/2}$ spectrum exhibits a strong peak and tail. The main peak was related to the Fe^{2+} bulk at 707.15 eV, and the tail includes the Fe^{2+} and Fe^{3+} multiplet splitting of the Fe $2p_{3/2}$ signal using the GS multiplet. The Fe^{2+} multiplets appear at 708−710 eV, whereas the Fe^{3+} multiplets appear at 710−714 eV. These multiplets correspond to the high-spin Fe^{2+} compounds at the surface sites and high-spin Fe^{3+} oxides.[39,41,46−48] These bands were also explained by the LFT,[27,41,42] which suggests that the oxides produced at the surface layer were removed *via* aqua regia etching.

2.2. Optical and Electrical Evaluations. Figure 6a presents the refractive index n and extinction coefficient k, whereas Figure 6b presents the optical absorption calculated from the k. The optical absorption coefficient $\alpha > 1 \times 10^5$ cm^{-1} for photon energy ($h\nu$) > 0.74 eV. The Tauc plot analysis was conducted using the results presented in Figure 6b. In the Tauc plot analysis, the intercepts of the linear extrapolations of the different slopes on the energy axis could be interpreted as optical transitions corresponding to those specific energy levels. The electronic behavior of $cFeS_2$ was controlled by the transitions of these energy levels. From Figure 7a, it can be seen that the estimated band gap is 1.0 eV, which is close to

https://doi.org/10.1021/acsomega.1c05232
ACS Omega 2021, 6, 31358−31365

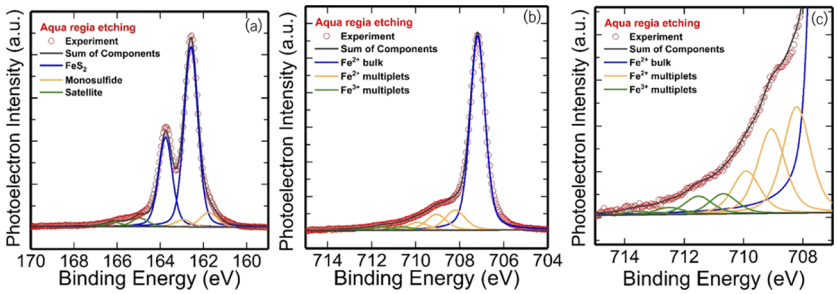

Figure 5. XPS spectrum of S 2p for $cFeS_2$ single crystals treated by both alcohol washing and aqua regia etching (a). XPS spectrum of Fe $2p_{3/2}$ for $cFeS_2$ single crystals treated by both alcohol washing and aqua regia etching (b). The magnified figure at a high-energy tail region of (c).

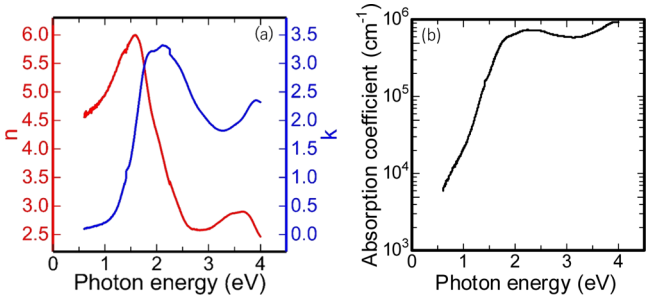

Figure 6. Refractive index (n) and extinction coefficient (k) of the $cFeS_2$ single-crystal wafer treated by the aqua regia solution (a). Optical absorption coefficient (α) calculated by k (b).

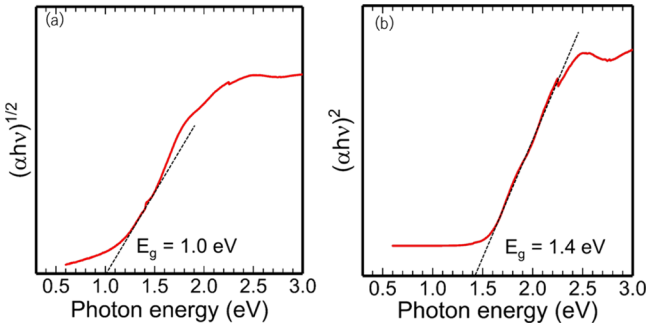

Figure 7. Tauc plot analysis of the $cFeS_2$ single-crystal wafer (a) with indirect band calculation (intercepted at 1.0 eV) and (b) with direct band calculation (intercepted at 1.4 eV).

the common value reported for $cFeS_2$,[1,5] despite the very limited fitting range (linearly changing range). This band gap value is estimated *via* linear fitting with $n = 1/2$ in the parameter $(\alpha h\nu)^n$ in the Tauc equation, which indicates that the estimated value is an indirect band gap. When $n = 2$ is used, which indicates a direct band gap, the estimated value is 1.4 eV, as presented in Figure 7b, with a relatively good fitting condition.

Figure 8 presents the photoluminescence (PL) spectra of $cFeS_2$ single-crystal wafers treated with alcohol washing or both alcohol washing and aqua regia etching. In both spectra, the emission intensity and peak position were similar, although they have relatively large noise owing to the room temperature measurement, and two peaks were observed at 1.316 and 1.358 eV. The emission intensity and peak position of the spectrum did not change even after aqua regia etching. This suggests that surface recombination was not influenced by the treatment, although the oxidation layer at the iron pyrite surface was removed by the aqua regia solution. In the two peaks of the PL

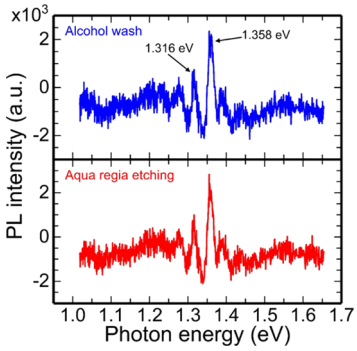

Figure 8. PL spectra of the $cFeS_2$ single-crystal wafer after the surface treatment.

spectrum, a sharp emission line was observed at 1.358 eV, and the energy difference between the two peaks was about 0.042 eV.

By calculating the wavenumber from the energy difference of 0.042 eV, the wavenumber was estimated to be 340 cm^{-1}, which is similar to the peak of the Raman spectrum in Figure 3. From the Raman spectrum, the S_2 vibration (E_{ge}) mode was observed at 343 cm^{-1}. This mode should be double degeneracy of the TO phonon and LO phonon. Therefore, the energy difference of the two peaks in the PL spectrum corresponds to the phonon energy obtained from the electron−phonon interaction. These results indicate that the two peaks are considered to be phonon replicas derived from the donor−acceptor pair emission. Such an indirect-to-direct transition in the $cFeS_2$ nanocube has also been observed by optical pump−probe studies.[22] In this study, we observed the electron transition by evaluating the optical absorption and PL of $cFeS_2$ single crystals. This indirect-to-direct transition is not unusual in semiconductors with a high density of defects and disorder phases, indicating the presence of the band tail below the conduction band, as shown in the disordered-phase-containing semiconductors.[22,49] The potential fluctuations derived from defects disturb the electronic band edges and result in the broadening of electronic states, which leads to the formation of band tails below the band edges. These discussions agree well with the report on the characterization of $cFeS_2$ nanocrystals in which the band tails were observed.[50]

Figure 9 presents the results of the conductivity and Hall coefficient at a temperature range of 50−300 K. Figure 9a presents the comparison between the measurement results of the reference data obtained *via* the Hall effect measurement using untreated $cFeS_2$ single crystals[29] and the measurement results of this study, in which oxide-layer-removed $cFeS_2$ single crystals were used. The conductivity variation behavior was

https://doi.org/10.1021/acsomega.1c05232
ACS Omega 2021, 6, 31358−31365

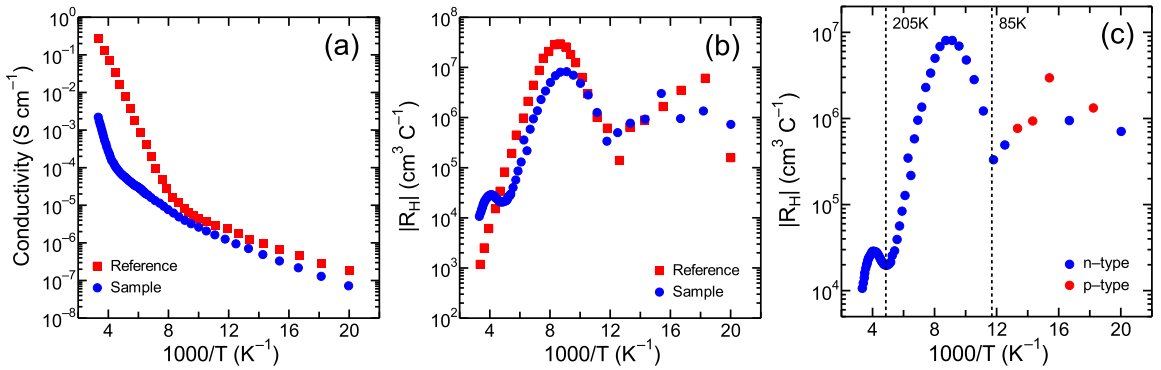

Figure 9. Results of the Hall effect measurement at a temperature range of 50−300 K for the $cFeS_2$ single crystal wafer treated by both alcohol washing and aqua regia etching. (a) Electrical conductivity, (b) absolute value of the Hall coefficient (R_H), and (c) absolute value of the R_H with carrier-type determination. The shown reference data[29] in (a,b) were replotted to compare with the data of this study.

found to be similar; however, the data in this study presented relatively smaller conductivity and different slopes in the high-temperature region (>120 K). Figure 9b shows the variation of the Hall coefficient. Based on the discussion in ref 30, this change in conductivity and Hall coefficient at intermediate temperatures is considered as surface conduction. Furthermore, the sign of the Hall effect measurement in Figure 9c shows that the sign of the Hall coefficient fluctuates between small positive and negative values. This is an artifact due to the hopping conduction origin of the surface state, which may cause an apparent inversion of the Hall signal.

In addition, the Hall mobility and carrier concentration calculated from the Hall coefficients are shown in Figure 10a,b, respectively. The mobility is smaller than that of other single-crystal data,[29,30] suggesting that it may be heavily compensated by impurities. One possibility of introducing these impurities derives from the purity of the source material. In this study, we note that the same conduction mechanism was obtained after removing the oxide layer from the $cFeS_2$ single crystal. This indicates that the oxidation of the $cFeS_2$ surface is not directly related to the surface conduction mechanism of $cFeS_2$. Although a recently discovered theoretical study of the high-pressure pyrite FeO_2 phase[51] suggested a possible Fe valence[52] that could support p-doping in $FeS_{2-x}O_x$, it is possible that another factor is responsible for the formation of the p-type surface inversion layer. The reduction of Fe−S coordination in the surface region was also observed in the S 2p spectrum of XPS after aqua regia etching in this study, suggesting that intrinsic surface states may be formed regardless of oxygen doping. We observed a dip around 205 K for the mobility and the carrier concentration as well. We still have not a clear mechanism, but we presume that the shallow defect states formed in the $cFeS_2$ influence these behaviors.

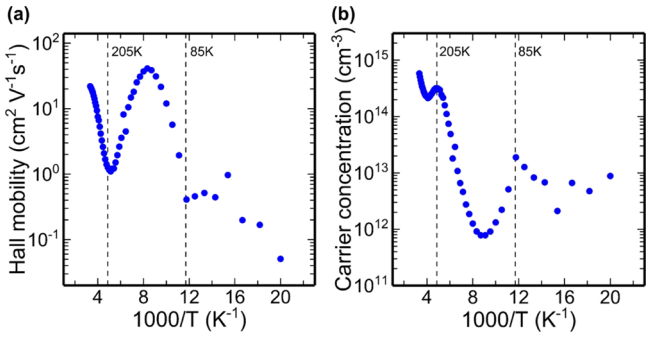

Figure 10. Hall mobility (a) and carrier concentration (b) calculated from the Hall coefficient data.

From the optical and electrical evaluation, controlling the surface and bulk conduction provides an understanding and improves the electrical properties for establishing an iron pyrite PV device. Voigt *et al.* have already demonstrated the increase in V_S by controlling the sulfur vapor during the growth of single crystals.[31] However, the method of decreasing V_S has not been employed yet due to the thermal instability of FeS_2,[53,54] which is the next challenge for this study.

3. CONCLUSIONS

In this study, we investigated the optical and electrical characteristics of cubic FeS_2 ($cFeS_2$) single crystals. $cFeS_2$ single crystals were prepared using the flux method. The oxidation production was inhibited by aqua regia etching. For the $cFeS_2$ wafer upon removing the surface oxide layer, the optical measurement confirmed the formation of $cFeS_2$ with an indirect band gap of 1.0 eV. The obtained Hall effect results suggested hopping conduction at a low-temperature range. In this study, the hopping conduction origin of the surface state was assumed even after the removal of the surface oxide layer formed after the wafer preparation, suggesting that the oxide layer has no strong impact on the surface conduction mechanism. Further understanding of the optical and electrical characteristics of $cFeS_2$ single crystals will pave the way for the PV application of FeS_2.

4. EXPERIMENTAL SECTION

4.1. Preparation of Iron Pyrite Crystals. Iron powder (purity: 99.9%, Kojundo Chemical Laboratory) was loaded on a quartz boat set in a quartz tube furnace; the sample was heated in a gas flow of 5% H_2/95% Ar at 300 °C for 15 h to remove the water and surface oxides. Sulfur powder (purity: 99%, FUJIFILM Wako Pure Chemical) was degassed and vacuum-dried in a borosilicate glass flask at 130 °C for 3 h. $Na_2S{\cdot}9H_2O$ (purity: 99%, FUJIFILM Wako Pure Chemical) was also dried and degassed in a Teflon beaker at 320 °C for 5 h, which produced a mixture of fine colorless and yellow powder, including Na_2S and polysulfides.

After the pretreatment, these materials were placed in alumina crucibles and sealed in evacuated quartz ampoules under a pressure of 4×10^{-3} Pa. About 0.51 g of iron powder (9.13 mmol), 0.98 g of Na_2S (12.56 mmol), and 1.21 g of sulfur powder (37.71 mmol) were placed in alumina crucibles.

https://doi.org/10.1021/acsomega.1c05232
ACS Omega 2021, 6, 31358−31365

These amounts were provided by the two diagrams of the Na−S binary phase and Fe−S binary phase.[55,56] Subsequently, the ampoule was placed in a muffle furnace and held vertically during the entire heat treatment period to prevent the contents of the crucible from mixing or spilling. The temperature of the ampoule was increased to 810 °C at a heating rate of 50 °C/h. When the temperature reached 300 and 400 °C, the ampoule was kept for 3 h at each temperature to prevent the quartz ampoule from bursting. When the temperature reached 810 °C, the ampoule was kept for 6 h to react with the materials in the alumina crucible. Then, the ampoule was cooled down to 600 °C in 240 h and finally to room temperature after 24 h.

The crucible was then removed from the ampoule and soaked in Millipore water for several hours to allow the flux to dissolve. After the removal of the crystals from the crucible, the crystals were rinsed with Millipore water and then dried. Consequently, the crystal ingots with a diameter of about 7 mm were obtained, as presented in Figure 1a. These ingots were then sliced using a SiC wheel saw and polished with emery papers (#100, #400, #800, #1200, and #200, Maruto Instrument). Moreover, they were mirror-finished using a polishing slurry containing diamond particles with an average particle size of 1.0 μm (Aqua diamond solution, Maruto Instrument) on a buff sheet (a hard type of polishing cloth, Maruto Instrument). Figure 1b presents the photograph of the crystal wafer after polishing. To remove the particles on the wafers, ultrasonic cleaning with acetone for 10 min was performed. Subsequently, the wafers were washed *via* ultrasonic cleaning with ethanol for 10 min. Finally, the wafers were etched by the aqua regia solution (HCl/HNO_3 = 3:1) diluted twofold by acetic acid for 1 min to remove the surface oxide layer and then immediately rinsed with ethanol. The samples were dried with nitrogen gas just before the characterization.

4.2. Characterizations. XRD measurement for phase identification was performed using RINT-TTR III (Rigaku Co.) with Cu Kα radiation. The tube voltage and tube current were 50 kV and 300 mA, respectively. The composition ratio of the obtained crystal wafers was evaluated using the EPMA (EPMA-1610, Shimadzu Co.). Moreover, the phase purity at the surface of the $cFeS_2$ single-crystal wafer was analyzed using a micro-Raman spectrometer NRS-4100 (Jasco Co.) at room temperature with a 50× objective lens and a 532 nm-wavelength excitation laser. XPS was performed using PHI 5000 VersaProbe II (ULVAC-PHI Inc.). The collected XPS spectra were analyzed using the ULVAC-PHI MultiPak software. All spectra were calibrated with the C 1s peak with a fixed value of 284.8 eV. After the calibration, the background from each spectrum was subtracted using the Shirley background to remove most of the extrinsic loss structures. To determine the stoichiometry of the compound, all survey scans were analyzed using the appropriate sensitivity factors. Spectroscopic ellipsometry was performed using HORIBA Jobin Yvon UVISEL ER AGMS-NSD to estimate the optical absorption of the $cFeS_2$ single-crystal wafer. The measured crystal wafer was treated with both alcohol washing and aqua regia etching. The measurement region was between 300 and 2100 nm. In the Tauc plot analysis, the intercepts of the linear extrapolations of the different slopes on the energy axis could be interpreted as an optical transition corresponding to the specific optical band gap. The electronic behavior of $cFeS_2$ is controlled by these energy gap transitions. Micro-PL using an excitation laser with a 635 nm wavelength and a spot size of a few μm was performed to investigate the electron transition in the band gap of $cFeS_2$. The spectra were analyzed using a grating monochromator and detected using a silicon charge-coupled device detector in the range of 750−1200 nm. The samples were set at room temperature under ambient air. The conductivity and Hall coefficient were measured from 50 to 300 K using ResiTest 8300 (Toyo Co.) with the Van der Pauw and DC method in a helium atmosphere. To prepare an ohmic contact, an Au thin film (200 nm in thickness) was deposited on the samples using the electron beam evaporation through a metal mask. To measure the resistivity and Hall coefficient, the applied current was adjusted from 0.1 μA at 50 K to 100 μA at 300 K.

AUTHOR INFORMATION

Corresponding Author

Yasuaki Ishikawa − *Graduate School of Materials Science, Nara Institute of Science and Technology, Ikoma, Nara 630-0192, Japan; College of Science and Engineering, Aoyama Gakuin University, Sagamihara, Kanagawa 252-5258, Japan;* orcid.org/0000-0003-4613-6117; Email: yishikawa@ee.aoyama.ac.jp

Authors

Shunsuke Uchiyama − *Graduate School of Materials Science, Nara Institute of Science and Technology, Ikoma, Nara 630-0192, Japan*

Ryosuke Sato − *Graduate School of Materials Science, Nara Institute of Science and Technology, Ikoma, Nara 630-0192, Japan*

Ryoji Katsube − *Department of Materials Science and Engineering, Kyoto University, Kyoto 606-8501, Japan;* orcid.org/0000-0003-4962-8547

Muhammad Monirul Islam − *Institute of Applied Physics, Graduate School of Pure and Applied Sciences, University of Tsukuba, Tsukuba, Ibaraki 305-8573, Japan;* orcid.org/0000-0002-9448-731X

Hideaki Adachi − *Graduate School of Materials Science, Nara Institute of Science and Technology, Ikoma, Nara 630-0192, Japan; Advanced Research Division, Panasonic Corporation, Kadoma, Osaka 571-8501, Japan*

Takeaki Sakurai − *Institute of Applied Physics, Graduate School of Pure and Applied Sciences, University of Tsukuba, Tsukuba, Ibaraki 305-8573, Japan;* orcid.org/0000-0001-5730-1937

Yoshitaro Nose − *Department of Materials Science and Engineering, Kyoto University, Kyoto 606-8501, Japan;* orcid.org/0000-0002-8320-1953

Complete contact information is available at: https://pubs.acs.org/10.1021/acsomega.1c05232

Funding

No funding to declare.

Notes

The authors declare no competing financial interest.

REFERENCES

(1) Ennaoui, A.; Fiechter, S.; Goslowsky, H.; Tributsch, H. Photoactive Synthetic Polycrystalline Pyrite (FeS_2). *J. Electrochem. Soc.* **1985**, *132*, 1579−1582.

(2) Ennaoui, A.; Tributsch, H. Energetic characterization of the photoactive FeS_2 (pyrite) interface. *Sol. Energy Mater.* **1986**, *14*, 461−474.

https://doi.org/10.1021/acsomega.1c05232
ACS Omega 2021, 6, 31358−31365

(3) Ennaoui, A.; Fiechter, S.; Pettenkofer, C.; Alonso-Vante, N.; Büker, K.; Bronold, M.; Höpfner, C.; Tributsch, H. Iron disulfide for solar energy conversion. *Sol. Energy Mater. Sol. Cells* **1993**, *29*, 289−370.
(4) Büker, K.; Alonso-Vante, N.; Tributsch, H. Photovoltaic output limitation of n-FeS_2 (pyrite) Schottky barriers: A temperature-dependent characterization. *J. Appl. Phys.* **1992**, *72*, 5721−5728.
(5) Altermatt, P. P.; Kiesewetter, T.; Ellmer, K.; Tributsch, H. Specifying targets of future research in photovoltaic devices containing pyrite (FeS_2) by numerical modelling. *Sol. Energy Mater. Sol. Cells* **2002**, *71*, 181−195.
(6) Wadia, C.; Alivisatos, A. P.; Kammen, D. M. Materials availability expands the opportunity for large-scale photovoltaics deployment. *Environ. Sci. Technol.* **2009**, *43*, 2072−2077.
(7) Fiechter, S.; Mai, J.; Ennaoui, A.; Szacki, W. Chemical vapour transport of pyrite (FeS_2) with halogen (Cl, Br, I). *J. Cryst. Growth* **1986**, *78*, 438−444.
(8) Höpfner, C.; Ellmer, K.; Ennaoui, A.; Pettenkofer, C.; Fiechter, S.; Tributsch, H. Stoichiometry-, phase- and orientation-controlled growth of polycrystalline pyrite (FeS_2) thin films by MOCVD. *J. Cryst. Growth* **1995**, *151*, 325−334.
(9) Thomas, B.; Cibik, T.; Höpfner, C.; Diesner, K.; Ehlers, G.; Fiechter, S.; Ellmer, K. Formation of secondary iron-sulphur phases during the growth of polycrystalline iron pyrite (FeS_2) thin films by MOCVD. *J. Mater. Sci. Mater. Electron.* **1998**, *9*, 61−64.
(10) Berry, N.; Cheng, M.; Perkins, C. L.; Limpinsel, M.; Hemminger, J. C.; Law, M. Atmospheric-pressure chemical vapor deposition of iron pyrite thin films. *Adv. Energy Mater.* **2012**, *2*, 1124−1135.
(11) Moon, D. G.; Rana, T. R.; Rehan, S.; Haider Naqvi, S. D.; Siddique, Y.; Lee, S. M.; Ahn, S. K.; Cho, Y. S.; Ahn, S. Na-Mediated Stoichiometry Control of FeS_2 Thin Films: Suppression of Nanoscale S-Deficiency and Improvement of Photoresponse. *ACS Appl. Mater. Interfaces* **2019**, *11*, 43244−43251.
(12) Samad, L.; Cabán-Acevedo, M.; Shearer, M. J.; Park, K.; Hamers, R. J.; Jin, S. Direct Chemical Vapor Deposition Synthesis of Phase-Pure Iron Pyrite (FeS_2) Thin Films. *Chem. Mater.* **2015**, *27*, 3108.
(13) Ares, J. R.; León, M.; Arozamena, N. M.; Sánchez-Páramo, J.; Celis, P.; Ferrer, I. J.; Sánchez, C. Evolution of the seebeck coefficient during the formation and crystallization of pyrite thin films. *J. Phys. Condens. Matter* **1998**, *10*, 4281−4289.
(14) Ares, J. R.; Ferrer, I. J.; Cuevas, F.; Sánchez, C. R. Growth of pyrite thin-films investigated by thermoelectric measurements. *Thin Solid Films* **2001**, *387*, 97−99.
(15) Ares, J. R.; Ferrer, I. J.; Sánchez, C. R. Majority carriers in pyrite thin films: An analysis based on Seebeck and Hall coefficient measurements. *Thin Solid Films* **2003**, *431−432*, 511−513.
(16) Soukup, R. J.; Prabukanthan, P.; Ianno, N. J.; Sarkar, A.; Kamler, C. A.; Sekora, D. G. Formation of pyrite (FeS_2) thin films by thermal sulfurization of dc magnetron sputtered iron. *J. Vac. Sci. Technol., A* **2011**, *29*, 011001.
(17) Bausch, S.; Sailer, B.; Keppner, H.; Willeke, G.; Bucher, E.; Frommeyer, G. Preparation of pyrite films by plasma-assisted sulfurization of thin iron films. *Appl. Phys. Lett.* **1990**, *57*, 25−27.
(18) Smestad, G.; Ennaoui, A.; Fiechter, S.; Tributsch, H.; Hofmann, W. K.; Birkholz, M.; Kautek, W. Photoactive thin film semiconducting iron pyrite prepared by sulfurization of iron oxides. *Sol. Energy Mater.* **1990**, *20*, 149−165.
(19) Cabán-Acevedo, M.; Faber, M. S.; Tan, Y.; Hamers, R. J.; Jin, S. Synthesis and properties of semiconducting iron pyrite (FeS_2) nanowires. *Nano Lett.* **2012**, *12*, 1977−1982.
(20) Bi, Y.; Yuan, Y.; Exstrom, C. L.; Darveau, S. A.; Huang, J. Air stable, photosensitive, phase pure iron pyrite nanocrystal thin films for photovoltaic application. *Nano Lett.* **2011**, *11*, 4953−4957.
(21) Kinner, T.; Bhandari, K. P.; Bastola, E.; Monahan, B. M.; Haugen, N. O.; Roland, P. J.; Bigioni, T. P.; Ellingson, R. J. Majority carrier type control of cobalt iron sulfide ($Co_xFe_{1-x}S_2$) pyrite nanocrystals. *J. Phys. Chem. C* **2016**, *120*, 5706−5713.
(22) Shukla, S.; Xing, G.; Ge, H.; Prabhakar, R. R.; Mathew, S.; Su, Z.; Nalla, V.; Venkatesan, T.; Mathews, N.; Sritharan, T.; Sum, T. C.; Xiong, Q. Origin of photocarrier losses in iron pyrite (FeS_2) nanocubes. *ACS Nano* **2016**, *10*, 4431−4440.
(23) Steinhagen, C.; Harvey, T. B.; Stolle, C. J.; Harris, J.; Korgel, B. A. Pyrite nanocrystal solar cells: Promising, or fool's gold? *J. Phys. Chem. Lett.* **2012**, *3*, 2352−2356.
(24) Moon, D. G.; Cho, A.; Park, J. H.; Ahn, S.; Kwon, H.; Cho, Y. S.; Ahn, S. Iron pyrite thin films deposited non-vacuum direct coating of iron-salt/ethanol-based precursor solutions. *J. Mater. Chem. A* **2014**, *2*, 17779−17786.
(25) Pettenkofer, C.; Jaegermann, W.; Bronold, M. Site specific surface interaction of electron donors and acceptors on FeS_2(100) cleavage planes. *Ber. Bunsen. Phys. Chem.* **1991**, *95*, 560−565.
(26) Bronold, M.; Pettenkofer, C.; Jaegermann, W. Surface photovoltage measurements on pyrite (100) cleavage planes: Evidence for electronic bulk defects. *J. Appl. Phys.* **1994**, *76*, 5800−5808.
(27) Bronold, M.; Tomm, Y.; Jaegermann, W. Surface states on cubic d-band semiconductor pyrite (FeS_2). *Surf. Sci.* **1994**, *314*, L931−L936.
(28) Bronold, M.; Büker, K.; Kubala, S.; Pettenkofer, C.; Tributsch, H. Surface preparation of FeS_2 electrochemical etching and interface formation with metals. *Phys. Status Solidi A* **1993**, *135*, 231−243.
(29) Limpinsel, M.; Farhi, N.; Berry, N.; Lindemuth, J.; Perkins, C. L.; Lin, Q.; Law, M. An inversion layer at the surface of n-type iron pyrite. *Energy Environ. Sci.* **2014**, *7*, 1974−1989.
(30) Walter, J.; Zhang, X.; Voigt, B.; Hool, R.; Manno, M.; Mork, F.; Aydil, E. S.; Leighton, C. Surface conduction in n-type pyrite FeS_2 single crystals. *Phys. Rev. Mater.* **2017**, *1*, 065403.
(31) Voigt, B.; Moore, W.; Manno, M.; Walter, J.; Jeremiason, J. D.; Aydil, E. S.; Leighton, C. Transport evidence for sulfur vacancies as the origin of unintentional n-type doping in pyrite FeS_2. *ACS Appl. Mater. Interfaces* **2019**, *11*, 15552−15563.
(32) Cabán-Acevedo, M.; Kaiser, N. S.; English, C. R.; Liang, D.; Thompson, B. J.; Chen, H.-E.; Czech, K. J.; Wright, J. C.; Hamers, R. J.; Jin, S. Ionization of high-density deep donor defect states explains the low photovoltage of iron pyrite single crystals. *J. Am. Chem. Soc.* **2014**, *136*, 17163−17179.
(33) Zhang, X.; Scott, T.; Socha, T.; Nielsen, D.; Manno, M.; Johnson, M.; Yan, Y.; Losovyj, Y.; Dowben, P.; Aydil, E. S.; Leighton, C. Phase stability and stoichiometry in thin film iron pyrite: Impact on electronic transport properties. *ACS Appl. Mater. Interfaces* **2015**, *7*, 14130−14139.
(34) Zhang, X.; Manno, M.; Baruth, A.; Johnson, M.; Aydil, E. S.; Leighton, C. Crossover From nanoscopic intergranular hopping to conventional charge transport in pyrite thin films. *ACS Nano* **2013**, *7*, 2781−2789.
(35) Zhang, X.; Li, M.; Walter, J.; O'Brien, L.; Manno, M. A.; Voigt, B.; Mork, F.; Baryshev, S. V.; Kakalios, J.; Aydil, E. S.; Leighton, C. Potential resolution to the doping puzzle in iron pyrite: Carrier type determination by Hall effect and thermopower. *Phys. Rev. Mater.* **2017**, *1*, 015402.
(36) Liang, D.; Cabán-Acevedo, M.; Kaiser, N. S.; Jin, S. Gated Hall Effect of Nanoplate Devices Reveals Surface-State-Induced Surface Inversion in Iron Pyrite Semiconductor. *Nano Lett.* **2014**, *14*, 6754−6760.
(37) Voigt, B.; Moore, W.; Maiti, M.; Walter, J.; Das, B.; Manno, M.; Leighton, C.; Aydil, E. S. Observation of an Internal p−n Junction in Pyrite FeS_2 Single Crystals: Potential Origin of the Low Open Circuit Voltage in Pyrite Solar Cells. *ACS Mater. Lett.* **2020**, *2*, 861−868.
(38) Kleppe, A. K.; Jephcoat, A. P. High-pressure Raman spectroscopic studies of FeS_2 pyrite. *Mineral. Mag.* **2004**, *68*, 433−441.
(39) Nesbitt, H. W.; Muir, I. J. X-ray photoelectron spectroscopic study of a pristine pyrite surface reacted with water vapour and air. *Geochim. Cosmochim. Acta* **1994**, *58*, 4667−4679.
(40) Mikhlin, Y.; Tomashevich, Y.; Vorobyev, S.; Saikova, S.; Romanchenko, A.; Félix, R. Hard X-ray photoelectron and X-ray

https://doi.org/10.1021/acsomega.1c05232
ACS Omega 2021, 6, 31358−31365

absorption spectroscopy characterization of oxidized surfaces of iron sulfides. *Appl. Surf. Sci.* **2016**, *387*, 796−804.
(41) Schaufuß, A. G.; Nesbitt, H. W.; Kartio, I.; Laajalehto, K.; Bancroft, G. M.; Szargan, R. Incipient oxidation of fractured pyrite surfaces in air. *J. Electron Spectrosc. Relat. Phenom.* **1998**, *96*, 69−82.
(42) Nesbitt, H. W.; Bancroft, G. M.; Pratt, A. R.; Scaini, M. J. Sulfur and iron surface states on fractured pyrite surfaces. *Am. Mineral.* **1998**, *83*, 1067−1076.
(43) Nesbitt, H. W.; Scaini, M.; Höchst, H.; Bancroft, G. M.; Schaufuss, A. G.; Szargan, R. Synchrotron XPS evidence for Fe^{2+}-S and Fe^{3+}-S surface species on pyrite fracture-surfaces, and their 3D electronic states. *Am. Mineral.* **2000**, *85*, 850−857.
(44) Gupta, R. P.; Sen, S. K. Calculation of multiplet structure of core p-vacancy levels. *Phys. Rev. B: Solid State* **1974**, *10*, 71−77.
(45) Gupta, R. P.; Sen, S. K. Calculation of multiplet structure of core p-vacancy levels. II. *Phys. Rev. B: Solid State* **1975**, *12*, 15−19.
(46) Mycroft, J. R.; Nesbitt, H. W.; Pratt, A. R. X-ray photoelectron and Auger electron spectroscopy of air-oxidized pyrrhotite: Distribution of oxidized species with depth. *Geochim. Cosmochim. Acta* **1995**, *59*, 721−733.
(47) McIntyre, N. S.; Zetaruk, D. G. X-ray photoelectron spectroscopic studies of iron oxides. *Anal. Chem.* **1977**, *49*, 1521−1529.
(48) Grosvenor, A. P.; Kobe, B. A.; Biesinger, M. C.; McIntyre, N. S. Investigation of multiplet splitting of Fe 2p XPS spectra and bonding in iron compounds. *Surf. Interface Anal.* **2004**, *36*, 1564−1574.
(49) Lazić, P.; Armiento, R.; Herbert, F. W.; Chakraborty, R.; Sun, R.; Chan, M. K. Y.; Hartman, K.; Buonassisi, T.; Yildiz, B.; Ceder, G. Low intensity conduction states in FeS_2: implications for absorption, open-circuit voltage and surface recombination. *J. Phys. Condens. Matter* **2013**, *25*, 465801.
(50) Lucas, J. M.; Tuan, C.-C.; Lounis, S. D.; Britt, D. K.; Qiao, R.; Yang, W.; Lanzara, A.; Alivisatos, A. P. Ligand-controlled colloidal synthesis and electronic structure characterization of cubic iron pyrite (FeS_2) nanocrystals. *Chem. Mater.* **2013**, *25*, 1615−1620.
(51) Hu, Q.; Kim, D. Y.; Yang, W.; Yang, L.; Meng, Y.; Zhang, L.; Mao, H.-K. FeO_2 and FeOOH under deep lower-mantle conditions and Earth's oxygen−hydrogen cycles. *Nature* **2016**, *534*, 241−244.
(52) Streltsov, S. S.; Shorikov, A. O.; Skornyakov, S. L.; Poteryaev, A. I.; Khomskii, D. I. Unexpected 3+ valence of iron in FeO_2, a geologically important material lying "in between" oxides and peroxides. *Sci. Rep.* **2017**, *7*, 13005.
(53) Birkholz, M.; Fiechter, S.; Hartmann, A.; Tributsch, H. Sulfur deficiency in iron pyrite (FeS_{2-x}) and its consequences for band-structure models. *Phys. Rev. B: Condens. Matter Mater. Phys.* **1991**, *43*, 11926−11936.
(54) Yu, L.; Lany, S.; Kykyneshi, R.; Jieratum, V.; Ravichandran, R.; Pelatt, B.; Altschul, E.; Platt, H. A. S.; Wager, J. F.; Keszler, D. A.; Zunger, A. Iron chalcogenide photovoltaic absorbers. *Adv. Energy Mater.* **2011**, *1*, 748−753.
(55) Sangster, J.; Pelton, A. D. The Na-S (sodium-sulfur) system. *J. Phase Equil.* **1997**, *18*, 89−96.
(56) Waldner, P.; Pelton, A. D. Thermodynamic modeling of the Fe-S system. *J. Phase Equilibria Diffus.* **2005**, *26*, 23−38.

https://doi.org/10.1021/acsomega.1c05232
ACS Omega 2021, 6, 31358−31365